

2. Synthesis method and experimental techniques

2.1 Introduction

The processing of ceramic materials has progressed from Potter's wheel to the modern age of innovative fields. Processing and synthesis of ceramic and other materials should be designed with specific attention to controlling and changing the chemical and physical properties for promising use in modern era emerging applications. Therefore, there is a need for special attention to various synthesis tools for processing, synthesizing, and evaluation of associated properties.

In the present thesis, the polycrystalline $\text{La}_2\text{Zr}_2\text{O}_7$ and $\text{Gd}_2\text{Zr}_2\text{O}_7$ ceramic compounds were prepared through a facile and economical synthesis approach, i.e., the standard solid-state method, which is one of the popular technique for the preparation of ceramic materials [1,2]. A brief description of materials, preparation of zirconate pyrochlore oxides via the solid-state method, and irradiation experiments are discussed. Moreover, the fabricated zirconate pyrochlore oxides pellets were characterized by powder X-ray diffraction (P-XRD) and Grazing incidence X-ray diffraction (GIXRD). Unit cell parameters of zirconate pyrochlore oxides were deduced Rietveld refinement using the FullProf program [3,4]. Microstructural study was performed using field emission scanning electron microscopy (FE-SEM) and compositional information about the prepared pellets were quantified using the energy-dispersive X-ray spectroscopy (EDX). The Raman spectroscopy was performed to examine the disorder, lattice defects, and distortion in vibrational modes. The deterioration of atomic ordering was investigated from high-resolution transmission electron microscopy. A brief description of above mentioned experimental techniques is also discussed here.

2.2 Preparation of $\text{La}_2\text{Zr}_2\text{O}_7$ and $\text{Gd}_2\text{Zr}_2\text{O}_7$ matrices

2.2.1 Materials

Lanthanum (III) oxide, La_2O_3 (99.90 %), zirconium (IV) oxide, ZrO_2 (99.0 %), and gadolinium (III) oxide Gd_2O_3 (99.9 %) were purchased from Sigma-Aldrich. The ethanol ($\text{C}_2\text{H}_5\text{OH}$) was purchased from Merck. All reagents were used without further purification. Lanthanum (III) oxide, zirconium (IV) oxide, and gadolinium (III) oxide were used as reagents. The high purity synthetic grade ethanol was used as a wet grinding aid.

2.2.2 Solid-state method

The solid-state process is a facile and economical synthesis method for the preparation of polycrystalline material. The solid-state method is a widely accepted technique and has several advantages such as low costs, simplicity in process and handling, reduced pollution, and easy mass production. All these factors are important in the industry for scaling up production [5].

This approach involves the mixing of reactants (in powder form) in stoichiometric ratio followed by several steps such as crushing, grinding, and milling till the formation of homogeneity. The prime object of the solid-state technique is the mingling of the precursors to the greatest extent of feasibility. Thus, this technique includes mingling of powder precursors and step by step annealing for a longer duration at elevated temperature followed by intermittent grinding in between for sublime homogeneity.

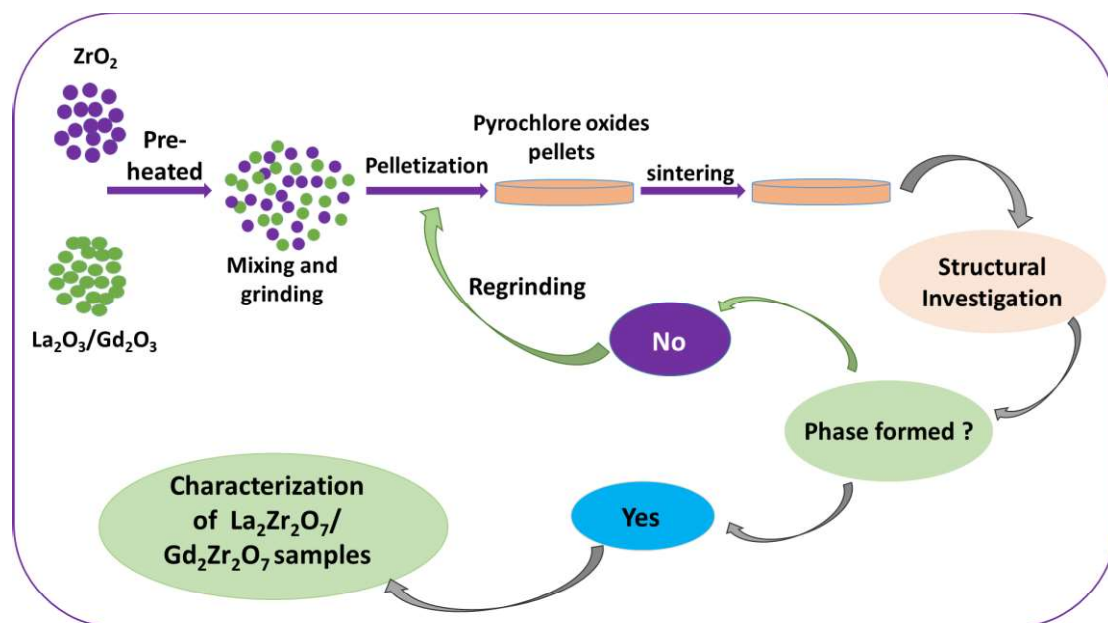


Figure 2.1 Schematic diagram of the synthesis process of $\text{La}_2\text{Zr}_2\text{O}_7$ and $\text{Gd}_2\text{Zr}_2\text{O}_7$ pyrochlore oxides.

2.2.3 Synthesis of $\text{La}_2\text{Zr}_2\text{O}_7$ and $\text{Gd}_2\text{Zr}_2\text{O}_7$

(a) $\text{La}_2\text{Zr}_2\text{O}_7$ preparation: $\text{La}_2\text{Zr}_2\text{O}_7$ samples were synthesized accounting the stoichiometric ratio of high purity La_2O_3 and ZrO_2 oxides. The lanthanide oxides are found extremely sensitive towards atmospheric CO_2 and H_2O . Therefore, in order to ensure the retention of the designed stoichiometries, and to decompose the existing carbonates and hydroxides; avoiding the volatile impurities and moisture, the reagents were heated at 1100°C for 6 h [6]. After pre-

heating, the stoichiometric ratio of the starting reactants (La_2O_3 and ZrO_2) was mixed followed by grinding. The grinding of reactants mixture has been performed thoroughly using high purity (synthetic grade) ethanol to achieve homogenization. Here, it is worth mentioning that we have prepared the two series of $\text{La}_2\text{Zr}_2\text{O}_7$ pyrochlore. In the first series (chapter 3), by thoroughly mixing and grinding reactants (La_2O_3 and ZrO_2), the pellets (10 mm) were prepared using the hydraulic press. The prepared pellets were annealed at 1200°C , 1300°C , and 1500°C with the extended annealing duration, i.e., 24, 48, and 96 h. In the second series (chapter-3 and chapter-4), after thoroughly grinding of reactants (La_2O_3 and ZrO_2) with a high extent of feasibility, the pellets were heated at 1200°C for 12 h. To achieve better homogeneity, the pellets were reground, pelletized, and annealed at 1500°C for 24 h.

(b) $\text{Gd}_2\text{Zr}_2\text{O}_7$ preparation: A similar synthesis approach was followed for $\text{Gd}_2\text{Zr}_2\text{O}_7$ with few modifications. Here, for the preparation of $\text{Gd}_2\text{Zr}_2\text{O}_7$ samples, the stoichiometric amount of Gd_2O_3 and ZrO_2 reactants were mixed and performed grinding to the extent of homogeneity. Upon thoroughly grinding, the pellets were prepared and annealed at 1200°C for 24 h. After first annealing, the pellets were ground and pelletized again, and annealed at 1300°C for 36 h. In order to achieve better uniformity and phase formation, the pellets after the second heating were ground, pelletized, and heated at 1400°C , and 1500°C for 48 h at atmospheric conditions [7]. The schematic diagram of $\text{La}_2\text{Zr}_2\text{O}_7$ and $\text{Gd}_2\text{Zr}_2\text{O}_7$ samples preparation is displayed in Fig. 2.1.

2.3 Irradiation Experiments

In this thesis, the $\text{La}_2\text{Zr}_2\text{O}_7$ samples were irradiated at two different temperatures (300 K and ~ 88 K) using 1.0 MeV Xe^{4+} ions and 500 KeV Kr^{2+} ions with the extension of ion fluence (1.0×10^{13} , 5.0×10^{13} , 1.0×10^{14} ions/cm²). Irradiation experiments were conducted at the LEIBF unit, Inter-University Accelerator Centre (IUAC), New Delhi. The schematic diagram of the irradiation process of zirconate pyrochlore oxides is presented in Fig. 2.2. The irradiation experiments chamber pressure was maintained at 10^{-7} mbar. All the samples were loaded using a tape on the target ladder to be placed inside the irradiation chamber, which can be controlled during the experiment by a ladder controlling unit and its live movement can be seen at the user end *via* camera set up in the irradiation unit as shown in Fig. 2.3.

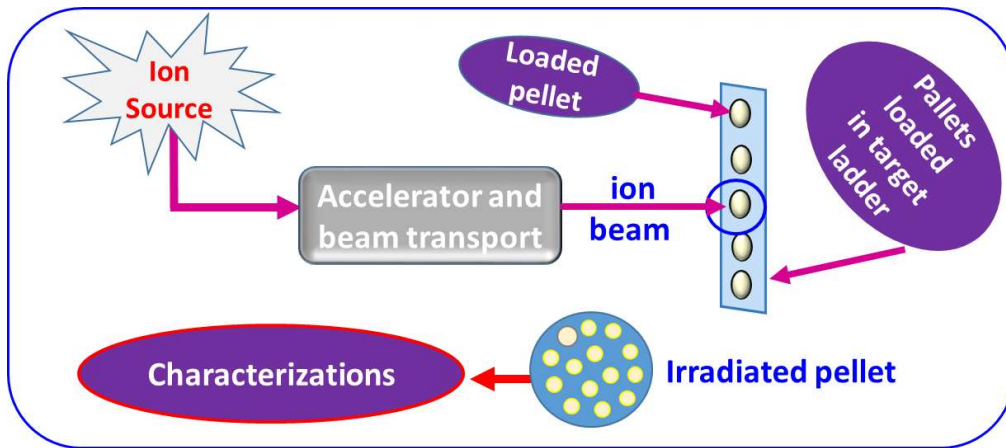


Figure 2.2 Schematic diagram of irradiation process of zirconate pyrochlore oxides ($\text{La}_2\text{Zr}_2\text{O}_7$ and $\text{Gd}_2\text{Zr}_2\text{O}_7$).

A focused normal ion beam hits the target samples at 90 degrees and performs raster scanning during the experiments. The irradiation ion beam was optimized for a $1.0 \times 1.0 \text{ cm}^2$ scanning area in the X-Y plane. Moreover, magnetic quadrupole and steerer magnets are used to focus the ion beam on the target sample. Further, the crystal of quartz material is kept on top of one of the sides of the target ladder. To ensure the desired beam size on the samples, the ion beam is first made to hit the quartz crystal and it is optimized before moving to target samples, i.e., $\text{La}_2\text{Zr}_2\text{O}_7$ samples.

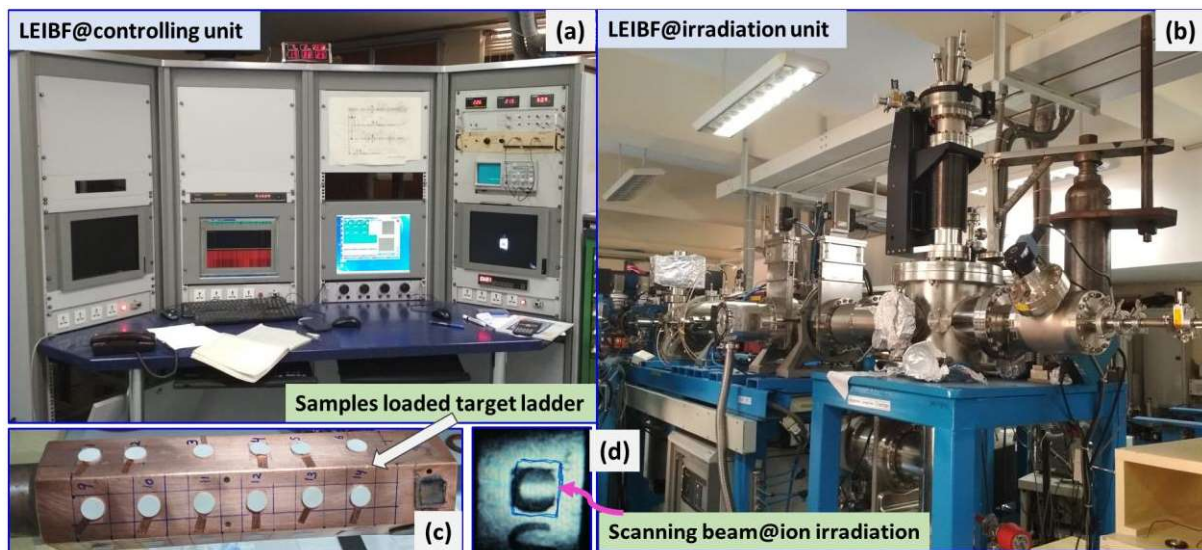


Figure 2.3 The real photograph of low energy ion beam controlling unit (a), irradiation unit (b), samples loaded target ladder (c), and (d) scanning ion beam during ion irradiation.

In a similar way, the $\text{Gd}_2\text{Zr}_2\text{O}_7$ samples were irradiated using 100 MeV I^{7+} ions at different fluences (1.0×10^{12} , 3.0×10^{12} , 1.0×10^{13} , 3.0×10^{13} , and $1.0 \times 10^{14} \text{ ions/cm}^2$). High energy ion irradiation experiments were performed at the 15UD pelletron accelerator facility,

a tandem electrostatic accelerator, IUAC, New Delhi, India. All samples were irradiated at room temperature under the vacuum of the order of 10^{-7} mbar.

Table 2.1 Represents the irradiation parameters of irradiated $\text{La}_2\text{Zr}_2\text{O}_7$ pyrochlore.

| Ion | Ion energy (MeV) | Fluence (ions/cm ²) | Dose (dpa) |
|------------------|------------------|---------------------------------|------------|
| Xe^{4+} | 1.0 | 1.0×10^{13} | 0.0026 |
| | | 5.0×10^{13} | 0.0130 |
| | | 1.0×10^{14} | 0.0260 |

The parameters used for the ion irradiation experiment were calculated by employing the software called SRIM (Stopping and Range of Ions in Matter) 2013 [8]. SRIM produces the results in the form of a table for stopping powers (nuclear and electronic stopping powers), ion straggling distribution, and the range of ions in the material/sample. The Monte Carlo algorithm in SRIM gives an approximate estimation of displacements/vacancies caused by energetic ions and ranges of bombarded ions. SRIM calculations were performed in full cascade mode to obtain an accurate approximation of the damage caused by energetic bombarded ions. All the atoms were set to 50 eV threshold displacement energy for 15000 ions for zirconate pyrochlore oxides [9].

The SRIM output files, Novac.txt, Vacancy.txt, and Range.txt helped to calculate the damage, i.e. called dpa (or displacement per atom by bombarded ion) defined as [10].

$$\alpha(\text{dpa}) = \frac{\epsilon(\text{ions/cm}^2) \times R(\text{displacement/ions/cm})}{\rho(\text{atoms/cm}^3)} \quad (2.1)$$

Where R is displacement per ion per cm and is obtained from vacancy.txt file from SRIM, ϵ is ion fluence and ρ is density in atom/cm³.

Further, for the particular fluence, the irradiation time was calculated using the expression.

$$T(\text{time}) = \frac{\text{ion fluence} \times \text{area of target sample (cm}^2\text{)}}{\text{current (pA)} \times (6.25 \times 10^9)} \quad (2.2)$$

Table 2.1 shows the ion fluence and dose (dpa) of $\text{La}_2\text{Zr}_2\text{O}_7$ upon irradiation of 1.0 MeV Xe^{4+} ions. Here, it is worth mentioning that there is energy loss to atomic nuclei and electrons in the compounds upon the interaction of energetic ions with solids. The nuclear energy loss dominates upon the interaction of low energy beam of ions ($E < 0.5$ MeV) with the solids and results in, elastic scattering collisions between atomic nuclei leading to the displacement of atoms in the system [11]. However, upon the interaction of high energetic ions ($E > 50$ MeV) with solids, the electronic energy loss dominates and results in, produce severe local ionization

which is a primary cause of track formation, damage production, damage recovery, track formation, and so on.

Table 2.2 The simulated value of S_e , S_n , and R_p for zirconated pyrochlore oxides for Xe^{4+} and I^{7+} ions.

| Xe ⁴⁺ (1.0 MeV) La ₂ Zr ₂ O ₇ | | | I ⁷⁺ (100 MeV) Gd ₂ Zr ₂ O ₇ | | |
|--|-------------------|---------------|---|-------------------|---------------|
| S_e (keV/nm) | S_n (keV/nm) | R_p (nm) | S_e (keV/nm) | S_n (keV/nm) | R_p (nm) |
| 1.12 | 2.90 | 210 | 20.10 | 0.17 | 9200 |

Moreover, the nuclear and electronic losses are found to be similar magnitude upon the interaction of intermediate energy ions ($0.5 <E> 50$ MeV) with solids. The interaction of intermediate energy ions with solids exhibits an additive impact on the recovery process and damage production and results in, affect the damage accumulation and evolution of nanostructures [11]. The electronic energy loss (S_e) and nuclear energy loss (S_n) and projectile range (R_p) of La₂Zr₂O₇ and Gd₂Zr₂O₇ were simulated using SRIM 2013. The simulated values of S_e , S_n , and R_p of respective compounds are summarized in Table 2.2.

2.4. Analytical characterization tools

2.4.1 X-ray diffraction (XRD)

Diffraction is one of the leading tools to investigate the materials to get information about the spatial arrangements of atoms conceived by Max von Laue in the year 1912 [12]. X-ray diffraction (XRD) is a non-destructive analytical tool for phase identification of crystalline material. The first experiment with single crystals of copper sulphate and zinc sulphite was performed by the Laue and his co-workers and stated that the crystalline substances act as three-dimensional diffraction gratings for X-ray wavelength. In 1916, Debye and Scherrer have recorded the first powder diffraction pattern [13]. XRD is often used to determine structural properties such as crystal structure, phase composition, preferred crystal orientation, lattice parameters, grain size, strain, crystal defects, *etc.* A divergent source of X-rays is focused on the flat plate sample which is then diffracted and collected by the detector. X-ray wavelengths are comparable to interatomic distances in molecules and crystals. According to Bragg's law, the incident X-ray beam interacts with the crystalline specimen and generates constructive interference [12].

$$2d\sin\theta = n\lambda \quad (2.3)$$

where, d is the distance between two adjoining planes, θ is the glancing angle, and λ is the X-ray wavelength.

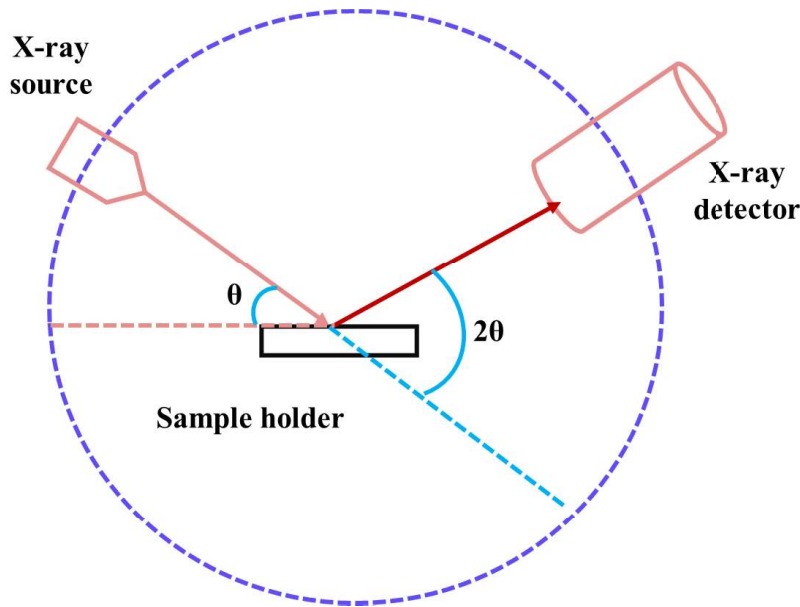


Figure 2.4 Represents the schematic diagram of different components of an XRD. The dotted circles represent the goniometer where the sample is placed in the center.

In the XRD technique, there is a measurement of the scattered intensity of an X-ray beam incident on a matrix [Fig. 2.4] and the intensity of the diffracted beam is deduced as a function of the diffraction angle (2θ). The experimentally acquired diffraction pattern of a specimen contains information about Bragg's scattering angle (2θ), which is the distinctive signature of the material. The reflections patterns recorded experimentally equated with the ICDD file, i.e., the international centre for diffraction data and factual findings of the material/compound presumed [14].

In this thesis, XRD measurements were recorded using the Rigaku Smart Lab and Bruker D8 advance X-ray diffractometer ($\lambda = 1.5406 \text{ \AA}$). The Debye Scherrer equation, $D = K\lambda/\beta\cos\theta$ was utilized to deduce the average crystallite size. Moreover, the average crystallite size and lattice strain of zirconate pyrochlore oxides were determined using the expression, $\beta = K\lambda/D\cos\theta + 4\epsilon \tan\theta$, which is called the Williamson-Hall equation. The W-H equation suggests that the peak broadening depends on the crystallite size and lattice strain. The Rietveld refinement of XRD patterns of $\text{La}_2\text{Zr}_2\text{O}_7$ and $\text{Gd}_2\text{Zr}_2\text{O}_7$ samples were refined

using the Fullprof program. During the Rietveld refinement process, the Pseudo-Voigt function was used in the fitting of XRD patterns.

2.4.2 Grazing Incidence X-ray Diffraction (GIXRD)

GIXRD is utilized for analyzing the upper irradiated thin (multi) layer (path length is short for X-rays) of the sample (or thin films analysis) via X-ray scattering. Fig. 2.5 shows the schematic configuration for GIXRD.

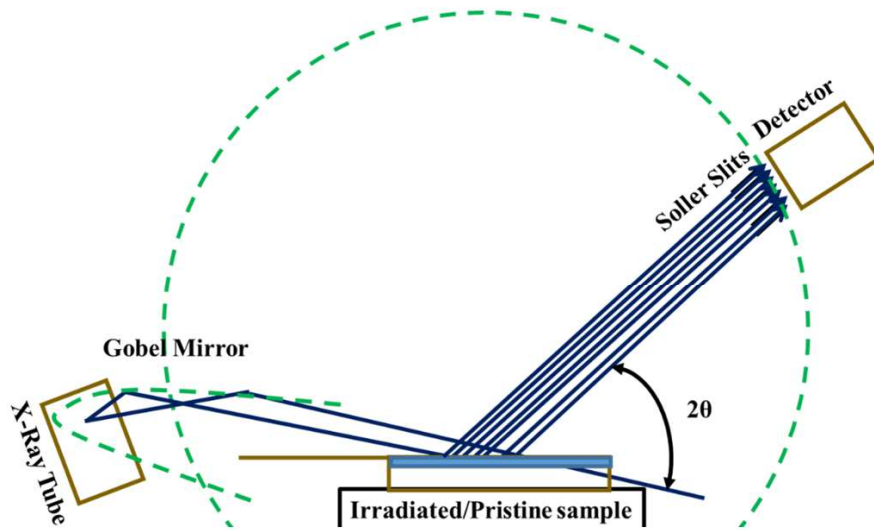


Figure 2.5 Schematic representation of the configuration of GIXRD.

In GIXRD, the X-rays penetrate the sample up to a fixed maximum depth defined by a fixed grazing angle made by tube w.r.t. sample. Each measurement by X-ray beam was completed after the alignment of the sample surface. A parallel X-ray beam is utilized to avoid the sample displacement errors due to discrepancies in sample alignment. As shown in Fig. 2.5, a parallel beam is produced by utilizing a Göbel mirror to transform the divergent primary beam produced by an X-ray tube. The low grazing incident angle is used to guide the penetration depth of X-rays in order to avoid the contribution of scattering from the substrate or un-irradiated layer of the sample. The optimized value of grazing angle can be determined by using the linear absorption coefficient (μ) and thickness (t) of the irradiated layer or thin-film as follows [15].

$$\theta = \sin^{-1} \mu t \quad (2.4)$$

The critical angle of total reflection should be lower than the grazing incidence angle; it depends on the sample and wavelength of X-rays from the source. At a low grazing angle, incident X-rays cover a large surface area of the sample; hence the surface of the sample gets X-rays on the same angle θ . The soller slits help to maintain a good 2θ resolution and allow the

detector to receive only those diffracted X-rays from the irradiated region which are in the direction of 2θ . Therefore, while recording the data, the incident X-ray beam is retained at grazing angle (can be calculated using the eq. 2.4) and the detector and solar slits scan the sample over the preferred angle 2θ . Hence, a diffraction pattern of the sample is recorded with a good 2θ resolution as specified by scanning steps and soller slits [15]. All samples patterns Rigaku Smart Lab X-ray diffractometer (CuK α source, $\lambda= 1.5406 \text{ \AA}$) was used to recorded the GIXRD pattrens.

2.4.3 Field Emission Scanning Electron Microscopy

FE-SEM is one of the most heavily used microscopic instruments in research areas owing to its exceptionally higher magnification, higher resolution, and ease of specimen inspection [16]. FE-SEM uses a beam of electrons to image the samples. A precise selection of electron energies over the desired range makes it possible to produce an image with high resolution. An FE-SEM consists of the following components: (a) an electron gun, (b) an electromagnetic lens system, (c) detectors, and (d) a stage or sample holder. The electron gun provides an intense beam of high-energy electrons. There are two types of guns, i.e., Thermionic gun and Field emission gun. The thermionic gun uses a heated filament to overcome the work function of the filament material, such that the electron can escape from the material itself. While the field emission gun uses a large electrical potential gradient across the filament to pull out the electrons. Fig. 2.6 illustrates the schematic of an electron-sample interaction in FE-SEM. The electron beam follows the vertical path through the column in the FE-SEM microscope and passes through the electromagnetic lenses that focus and direct the beam down towards the sample. The high-energy electrons upon interaction with the samples undergo either elastic scattering with the atomic nucleus or inelastic scattering with the atomic electrons. The secondary electrons (SEs), backscattered electrons (BSEs), and characteristics X-rays are produced upon electron sample interaction. Detectors are employed to detect these SE electrons, BSE electrons, and X-rays. The modern FE-SEM (ultra-high resolution $\sim 1.0 \text{ nm}$, magnification $\sim \times 1,000,000$) is far better than conventional scanning electron microscopes. Therefore, higher resolution magnification, larger depth of field, compositional information and user-friendliness of the apparatus, and general simplicity of the image interpretation make the FE-SEM one of the most heavily used instruments for research purposes.

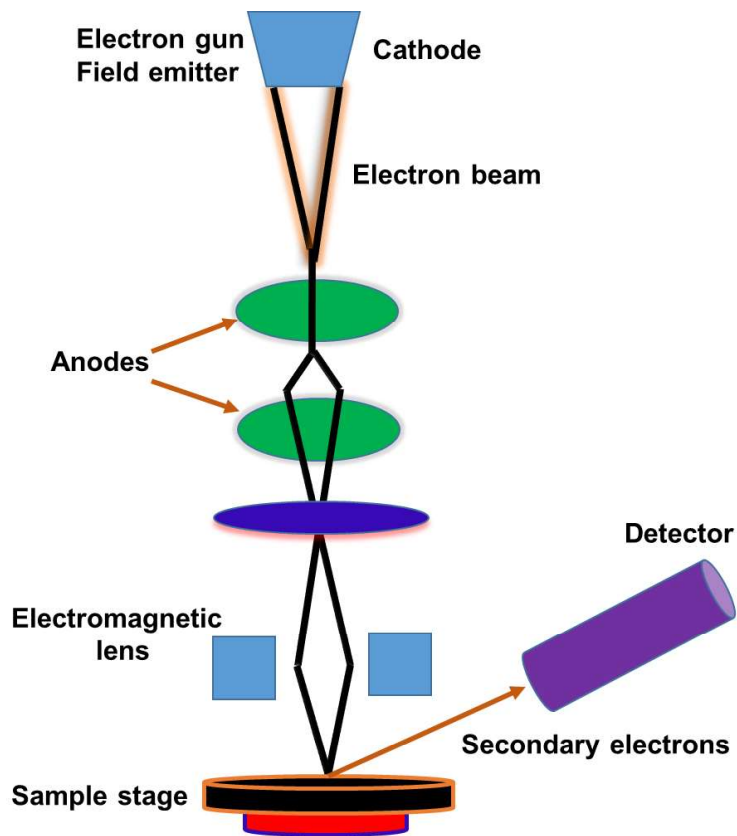


Figure 2.6 Schematic representation of electron-sample interaction in an FE-SEM.

To avoid the charging phenomenon, the thin layer of gold/palladium was coated on samples using magnetron sputtering. The microstructure of $\text{La}_2\text{Zr}_2\text{O}_7$ and $\text{Gd}_2\text{Zr}_2\text{O}_7$ samples are investigated by field emission scanning electron microscopy (FESEM, Supra 55 Zeiss, UK). The system is also equipped with EDS analyzer (Oxford Instruments, UK), which is used for compositional analysis of samples.

2.4.4. Raman spectroscopy

Raman spectroscopy technique is non-destructive and sensitive to local disorder, lattice defects, and metal-oxygen vibrational mode conditions. It is based on the Raman Effect, discovered by the C.V. Raman in 1928 [17] and got the Nobel Prize in 1930. It states that “when a monochromatic beam is scattered from the specimen, the scattered radiation shows a difference in the wavelength. This outcome is distinctive to the molecule that causes it and can be employed for spectroscopy analysis. The scattering procedure can take place either inelastically or elastically. If wavelength and frequency of the scattered photon are equal to incident photons (*elastic process*), called “*Rayleigh scattering*”. If there is a change in frequency and wavelength of the scattered photons (*inelastic scattering*), called the “*Raman Effect*”. A change in the energy between in-elastically scattered and incident photons is termed

as “*Raman shift*”. *Raman Effect* arises when the electric field vector of the incident photon interacts with the electric dipole of the molecule.

The higher frequency scattered photon from an incident beam is referred to as *anti-stokes scattering*, while lower frequency scattered photon is referred to as *stokes scattering* [Fig. 2.7]. The Raman shift is not affected by the frequency of the incident light, but it is a property of the substance that causes the *Raman Effect*. Raman spectrum is a plot of the intensity of the inelastically scattered photons *versus* change in energy.

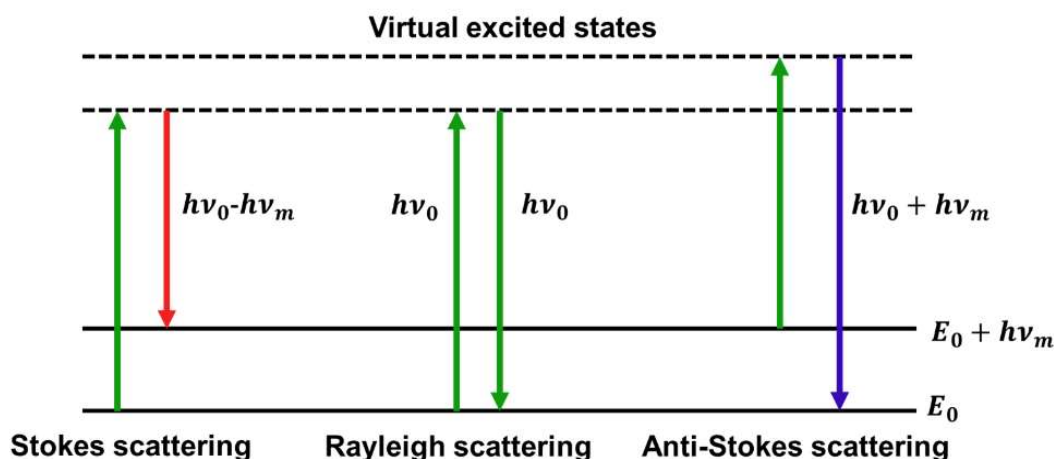


Figure 2.7 Illustration of Rayleigh, Stokes, and anti-Stokes scattering.

Raman Effect is based on the polarizability of the molecules as per classical theory. The induced dipole moment is proportional to the molecular polarizability (α) and electric field strength (E). If there is a change in molecular polarizability of system/molecules *via* vibration, then molecular vibration is called Raman active [18].

$$\left(\frac{d\alpha}{dQ}\right) \neq 0 \quad (2.5)$$

where α is the molecular polarizability which is a measure of how an electron cloud around a molecule can be distorted, Q is the normal coordinate of the displacements. Like Raman spectroscopy, FTIR spectroscopy is also a form of vibrational spectroscopy, but the interaction of radiation with matter is quite different in FTIR spectroscopy. The infra-red (IR) band arises due to a change in the dipole moment of the molecule upon interaction with the incident photon energy. For an IR active vibration, there must be a net change in permanent dipole moment during the vibration [19]

$$\left(\frac{d\mu}{dQ}\right) \neq 0 \quad (2.6)$$

Where μ is the dipole moment of the molecule. Some of the Raman active modes are forbidden in IR, and some vibrations modes are active for both Raman and IR.

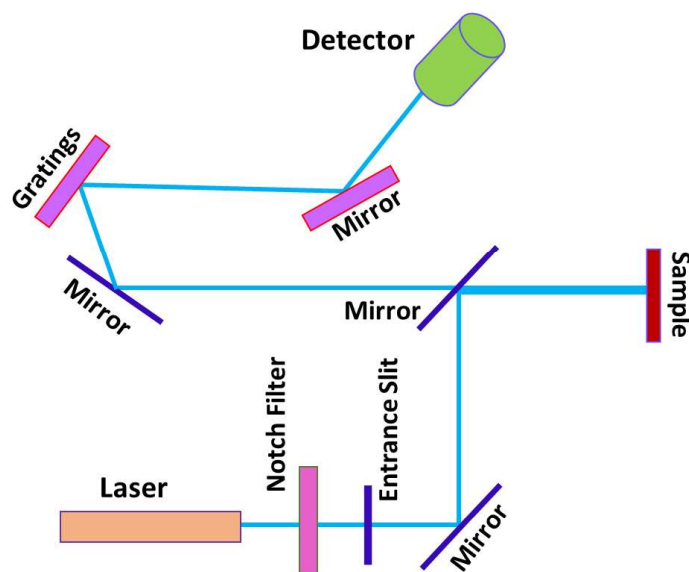


Figure 2.8 Schematic diagram of a Raman spectrometer.

There are several advantages of Raman over FTIR spectroscopy. For example, water is the strong absorber for IR, and it is a rather weak Raman scatterer. Figure 2.8 shows the typical schematic diagram Raman spectrometer The modern instrument typically consists of the NdYAG, Ar⁺, and Kr⁺ laser as a light source, because it gives a very narrow, highly monochromatic, and coherent beam. The focused laser beam is incident on the sample, and incident light scatters from the sample and passes through a grating monochromator. A sensitive photomultiplier measures the signal and after amplification, it is usually processed by a computer, and the final plot of the Raman spectrum is shown on the computer display. Raman measurements of all samples presented here were performed using a micro-Raman model STR 500 with an excitation (wavelength of 785 nm) from an Nd-YAG laser source and argon laser source equipped Labram-HR 800 spectrometer (488 nm).

2.4.5. High-resolution transmission electron microscopy (HR-TEM)

Transmission electron microscope (TEM) is an important tool for materials characterization [20]. TEM provides information about the particle size, morphology, defects, and interfaces state with high resolution [21]. Generally, two types of sources are used in TEM, i.e., thermionic or field emission source which may be tungsten filament or lanthanum hexaboride (LaB₆). The thermionic source has relatively poor qualities in comparison of corresponding field emission.

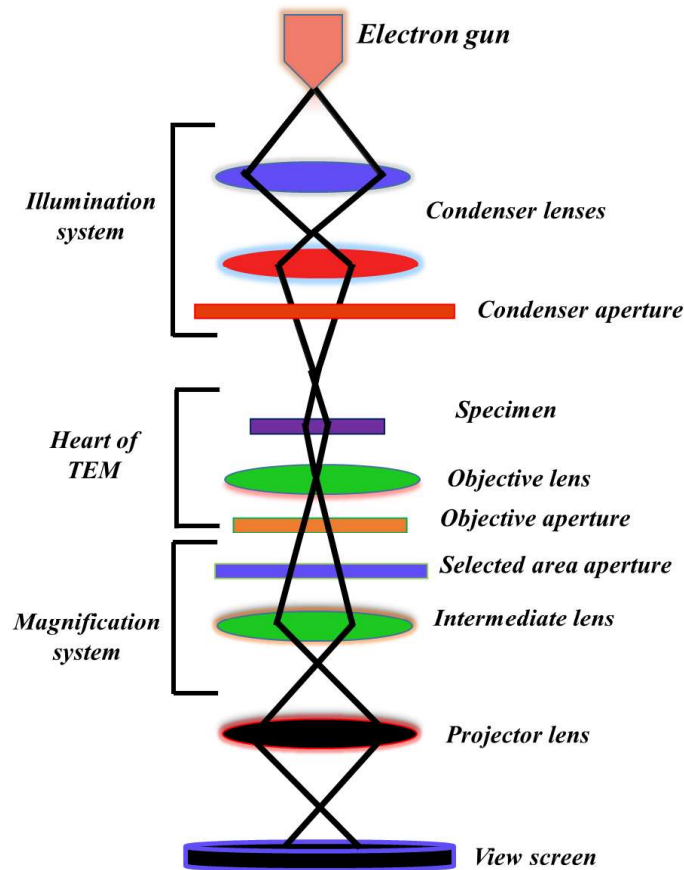


Figure 2.9 Schematic representation of electron-sample interaction in a TEM.

The field emission source has high current density and beam coherence which provide the ultra-high-resolution that is unique for performing experiments because it possesses coherence such as imaging. An illumination system consists of an emission source, condenser lenses, and a condenser aperture. The objective lenses focus the beam after passing through the specimen and capture an image of the specimen. The objective lens has two apertures, the first one is located in the back focal plane of the objective lens, which is used to select a particular diffraction beam to form the final image and adjust the image contrast. The second aperture is placed on the intermediate image plane and used to select the area of interest of the specimen to form the diffraction pattern. The magnification system consists of the projector and intermediate lenses. The projector and intermediate lenses magnify the image, captured from the objective lens, and produce the final image on the screen. A schematic representation of electron beam and specimen interaction is shown in Fig. 2.9. A TEM is equipped with various probing techniques such as EESL, STEM, ESD, *etc.* STEM is used for the morphological analysis of the samples whereas EDS, EELS, and HAADF are utilized for the elemental mapping as well as imaging based on contrast resulting from different elements constituting the sample [20]. TEM can be operated in different modes to acquire various information from the specimen. High-resolution transmission electron microscopy

(HR-TEM) is an inevitable technique for the high-resolution studies of compounds such as crystal structure, lattice defects, lattice fringes, and grain boundaries on the atomic scale. The sample should be beam insensitive, and appropriate caution must be taken during the preparation of the samples, such as surface cleaning, and conducting ability of the sample. The JEOL 3010 high-resolution transmission electron microscope (HRTEM) is used to characterize the samples.

References

- [1] G. Sattonnay, S. Moll, L. Thomé, C. Decorse, C. Legros, P. Simon, J. Jagielski, I. Jozwik, I. Monnet, Phase transformations induced by high electronic excitation in ion-irradiated $\text{Gd}_2(\text{Zr}_x\text{Ti}_{1-x})_2\text{O}_7$ pyrochlores, *J. Appl. Phys.* 108 (2010) 103512. <https://doi.org/10.1063/1.3503452>.
- [2] X. Shu, L. Fan, Y. Xie, W. Zhu, S. Pan, Y. Ding, F. Chi, Y. Wu, X. Lu, Alpha-particle irradiation effects on uranium-bearing $\text{Gd}_2\text{Zr}_2\text{O}_7$ ceramics for nuclear waste forms, *J. Eur. Ceram. Soc.* 37 (2017) 779–785. <https://doi.org/10.1016/j.jeurceramsoc.2016.09.034>.
- [3] Y. Kumar, P.M. Shirage, Highest coercivity and considerable saturation magnetization of CoFe_2O_4 nanoparticles with tunable band gap prepared by thermal decomposition approach, *J. Mater. Sci.* 52 (2017) 4840–4851. <https://doi.org/10.1007/s10853-0160719-5>.
- [4] Y. Kumar, A.K. Rana, P. Bhojane, M. Pusty, V. Bagwe, S. Sen, P.M. Shirage, Controlling of ZnO nanostructures by solute concentration and its effect on growth, structural and optical properties, *Mater. Res. Express.* 2 (2015) 105017. <https://doi.org/10.1088/2053-1591/2/10/105017>.
- [5] Z. Wang, G. Zhou, D. Jiang, S. Wang, Recent development of $\text{A}_2\text{B}_2\text{O}_7$ system transparent ceramics, *J. Adv. Ceram.* 7 (2018) 289–306. <https://doi.org/10.1007/s40145-018-0287-z>.
- [6] A.F. Fuentes, S.M. Montemayor, M. Maczka, M. Lang, R.C. Ewing, U. Amador, A Critical Review of Existing Criteria for the Prediction of Pyrochlore Formation and Stability, *Inorg. Chem.* 57 (2018) 12093–12105. <https://doi.org/10.1021/acs.inorgchem.8b01665>.
- [7] B.P. Mandal, N. Garg, S.M. Sharma, A.K. Tyagi, Solubility of ThO_2 in $\text{Gd}_2\text{Zr}_2\text{O}_7$ pyrochlore: XRD, SEM and Raman spectroscopic studies, *J. Nucl. Mater.* 392 (2009) 95–99. <https://doi.org/10.1016/j.jnucmat.2009.03.050>.
- [8] S. Liu, T. Yang, J. Zhang, Z. Yan, Y. Lu, D. Han, C. Wang, Y. Fang, Y. Wang, Thermal effects in ion irradiated Ti_2AlC and Ti_3SiC_2 , *Nucl. Instruments Methods Phys. Res. Sect. B Beam Interact. with Mater. Atoms.* 435 (2018) 50–55. <https://doi.org/10.1016/j.nimb.2017.10.006>.
- [9] T.C. Kaspar, J.G. Gigax, L. Shao, M.E. Bowden, T. Varga, V. Shutthanandan, S.R. Spurgeon, P. Yan, C. Wang, P. Ramuhalli, C.H. Henager, Damage evolution of ion

- irradiated defected-fluorite $\text{La}_2\text{Zr}_2\text{O}_7$ epitaxial thin films, *Acta Mater.* 130 (2017) 111–120. <https://doi.org/10.1016/j.actamat.2017.01.012>.
- [10] K. Liu, K. Zhang, T. Deng, B. Luo, H. Zhang, Heavy-ion irradiation effects of $\text{Gd}_2\text{Zr}_2\text{O}_7$ nanocrystalline ceramics as nuclear waste immobilization matrix, *J. Nucl. Mater.* 538 (2020) 152236. <https://doi.org/10.1016/j.jnucmat.2020.152236>.
- [11] W.J. Weber, D.M. Duffy, L. Thomé, Y. Zhang, The role of electronic energy loss in ion beam modification of materials, *Curr. Opin. Solid State Mater. Sci.* 19 (2015) 1–11. <https://doi.org/10.1016/j.cossms.2014.09.003>.
- [12] B. D. Cullity and S. R. Stock, *Elements of X-Ray Diffraction*, in: ISBN13:978-1-269-37450-7, 3rd Editio, Pearson Education Limited, 2014: pp. 1–641.
- [13] M. Etter, R.E. Dinnebier, A Century of Powder Diffraction: a Brief History, *Zeitschrift Für Anorg. Und Allg. Chemie.* 640 (2014) 3015–3028. <https://doi.org/10.1002/zaac.201400526>.
- [14] A.A. Bunaciu, E. gabriela Udriștioiu, H.Y. Aboul-Enein, *X-Ray Diffraction: Instrumentation and Applications*, *Crit. Rev. Anal. Chem.* 45 (2015) 289–299. <https://doi.org/10.1080/10408347.2014.949616>.
- [15] B.B. He, *Two dimensional X-ray diffraction*, in: ISBN 9781119356066, 2rd Editio, John Wiley & Sons, Inc., 2018: pp. 1–453.
- [16] K.D. Vernon-Parry, *Scanning electron microscopy: an introduction*, *III-Vs Rev.* 13 (2000) 40–44. [https://doi.org/10.1016/S0961-1290\(00\)80006-X](https://doi.org/10.1016/S0961-1290(00)80006-X).
- [17] C. V. RAMAN, K.S. KRISHNAN, A New Type of Secondary Radiation, *Nature.* 121 (1928) 501–502. <https://doi.org/10.1038/121501c0>.
- [18] J.M. Hollas, *Modern Raman spectroscopy*, in: ISBN 0 470 84416 7, 4th Editio, John Wiley & Sons Ltd, 2004: pp. 1–428.
- [19] E. Smith, G. Dent, *Resonance Raman Scattering A pratical Approach*, in: *Mod. Raman Spectrosc.*, John Wiley & Sons, Ltd, Chichester, UK, 2019: pp. 101–117.
- [20] D. B. Williams and C. B. Carter, *Transmission electron microscopy*, in: ISBN 978-0-387-76501-3, Springer, 2011: pp. 333–350.
- [21] B. Fultz, J. Howe, *Transmission electron microscopy and diffractometry of materials*, in: ISBN 978-3-540-73885-5, 3rd Editio, Springer Science & Business Media, 2012: pp. 1–771.